Sonar Observation of Heat Flux of Diffuse Hydrothermal Flows

Darrell Richard Jackson[1], Karen G Bemis[2], Guangyu Xu[3], and Anatoliy Ivakin[4]

[1]Applied Physics Laboratory
[2]Rutgers University
[3]Applied Physics Laboratory at University of Washington
[4]University of Washington

November 24, 2022

Abstract

Previous work using multibeam sonar to map diffuse hydrothermal flows is extended to estimate the heat output of diffuse flows. In the first step toward inversion, temperature statistics are obtained from sonar data and compared to thermistor data in order to set the value of an empirical constant. Finally, a simple model is used to obtain heat-flux density from sonar-derived temperature statistics. The method is applied to data from the Cabled Observatory Vent Imaging Sonar (COVIS) deployed on the Ocean Observatories Initiative's Regional Cabled Array at the ASHES vent field on Axial Seamount. Inversion results are presented as maps of heat-flux density in MW/m^2 and as time series of heat-flux density averaged over COVIS' field of view.

Sonar Observation of Heat Flux of Diffuse Hydrothermal Flows

Darrell Jackson[1], Karen Bemis[2], Guangyu Xu[1], and Anatoliy Ivakin[1]

[1]Applied Physics Laboratory, University of Washington.

[2]Department of Marine and Coastal Sciences, Rutgers University

Corresponding author: Darrell Jackson (drj12@uw.edu)

Key Points:

- Multibeam sonar is used to observe heat flux of diffuse hydrothermal flows.
- The inversion method estimates vertically-averaged temperature fluctuation.
- Validation and calibration of method by direct measurement is needed.

Abstract

Previous work using multibeam sonar to map diffuse hydrothermal flows is extended to estimate the heat output of diffuse flows. In the first step toward inversion, temperature statistics are obtained from sonar data and compared to thermistor data in order to set the value of an empirical constant. Finally, a simple model is used to obtain heat-flux density from sonar-derived temperature statistics. The method is applied to data from the Cabled Observatory Vent Imaging Sonar (COVIS) deployed on the Ocean Observatories Initiative's Regional Cabled Array at the ASHES vent field on Axial Seamount. Inversion results are presented as maps of heat-flux density in MW/m^2 and as time series of heat-flux density averaged over COVIS' field of view.

1 Introduction

This article extends the work reported in [Xu et al. 2021] with the goal of quantifying the heat output from a portion of the ASHES Vent Field on Axial Seamount. The earlier article gives references to the literature as well as a detailed description of the data provided by the Cabled Observatory Vent Imaging Sonar (COVIS). Diffuse discharges take many forms and may originate from the sides of sulfide mounds, isolated cracks, lava tubes, and areas of permeable seafloor [*Bemis et al*., 2012, Fig. 1], [*Barreyre et al*., 2012]. The heat output of diffuse-flow discharge may equal or exceed that of focused flow from associated smokers [*Barreyre et al*., 2012], [*Rona and Trivett*, 1992], [*Schultz et al*., 1992], [*Veirs et al*., 2006]. Shultz et al. [1992] used an electromagnetic-based flowmeter and several thermistors on the sulfide mound called Peanut in the southern half of Main Endeavour Field (MEF) to simultaneously measure temperature and vertical velocity in diffuse discharge for about two months estimating a diffuse heat-flux density of 2.91±0.23 MW/m^2. Trivett and Williams [1994] used thermistor moorings and tripod-mounted current meters to estimate heat flux from diffuse-flow regions on the Southern Juan de Fuca Ridge, obtaining a net flux of 125 ± 75 MW for the most active region. Their instruments were placed at a distance from the diffuse-flow regions of interest and relied on currents to convect the warm water toward their apparatus Viers et al. [2006], using data from an ROV, a CTD, and current meters, estimated the along-axis heat flux at MEF to be 8-42 MW. They concluded that the MEF heat flux was about equally divided between focused and diffuse flows. More recently, acoustic estimates of areal extent were combined with limited temperature and flow rate measurements to estimate heat transport by diffuse discharge at North Tower of the sulfide mound Grotto in MEF as 33-380 MW or a heat flux of 0.33-3.8 MW/m^2 over the 100 m^2 summit of the North Tower [*Rona et al*., 2015].

Observations of hydrothermal flows for the northern part of ASHES were reported in previous studies. Rona and Trivett [1992] conducted a thermal survey over a 100 m by 100 m area enclosing the depression region using a remotely operated vehicle (ROV) carrying a 1-m long vertical thermistor array. They estimated the heat output from both focused and diffuse flow sources to be 2.4-6.4 MW and 15-75 MW, respectively, from in-situ temperature measurements, which suggested diffuse flow venting was the dominant hydrothermal heat source at ASHES. Pruis and Johnson [2004] measured the flow rate and temperature of the discharge from a diffuse-flow source in ASHES using a fluid sampler cemented to the seafloor. They estimated a volume flux of 48 m^3/yr and a heat flux of 260 W/m^2 for the 1 m^2 area sealed by the sampler. Most recently, Mittelstaedt et al., [2016] measured heat flux of diffuse flow venting from a narrow fracture near the southern end of the depression region using the Diffuse Effluent

Measurement System (DEMS), which is a camera system augmented with thermistors that can measure the flow rate and temperature of diffuse-flow effluents. They obtained an estimated heat-flux density of 0.07-0.51 MW/m^2, which was subsequently extrapolated over all the cracks detected in a photomosaic survey to get a total heat flux from venting fractures of 0.1-4 MW.

With the exception of [*Trivett and Williams*, 1994], previous work either provides time series at specific points or large-scale snapshots of heat flux. The uncertainty in these measurements is great, with the ratio of upper to lower bounds being as large as 5 or 10. These facts motivate the present attempt to use multibeam sonar to estimate heat flux across substantial areas over long times.

The Cabled Observatory Vent Imaging Sonar (COVIS) was installed in July 2018 on the Ocean Observatories Initiative (OOI) Regional Cabled Array at the ASHES vent field on Axial Seamount. The resulting data have been used to obtain time series of diffuse-flow activity, primarily through estimation of the area of diffuse flow regions [*Xu et al*., 2021]. The present effort seeks to extend this work and that of [*Jackson et al.,* 2017], to provide a method for sonar observation of the heat output of diffuse flows. In Sect. 2, the thermistor data used as ground-truth are described, and, in Sect. 3, sonar data are discussed, and the first stage of inversion used to estimate temperature statistics is developed. Section 4 compares inverted and directly measured temperature statistics, and the final stage of inversion for heat-flux density is developed in Sect. 5. Inversion results for heat flux are given in Sect. 6, and Sect. 7 offers conclusions and discusses outstanding issues.

2 Thermistor Data

The thermistor array pictured in Fig. 1 was set on the seafloor by ROV Jason at the two sites shown in Fig. 2. The thermistors are RBRsolo T, with response time of 0.1 s, consistent with the sonar ping-to-ping spacing of 0.25 s. At sites 1H and 4C several stations were occupied on June 6, 2019, with nominal 25-cm spacing. Seven stations were occupied at 1H and eleven at 4C. The multiple stations give information on the spatial variability and on spatial averages of temperature.
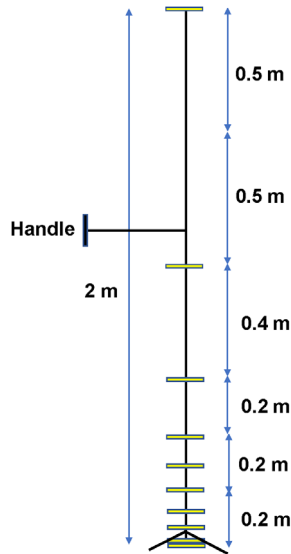
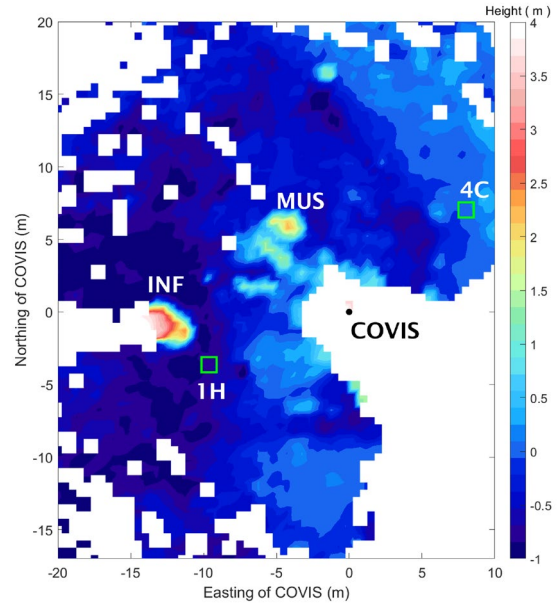*Figure 1. Sketch of thermistor array used for ground-truth measurements.*

Figure 2. Sites in ASHES vent field where thermistor arrays were deployed in 2018 and 2019. Sites 1H and 4C are marked by green squares. COVIS's location is marked by a black dot. The smaller bathymetric feature to the NW of COVIS is the Mushroom black smoker and the larger one to the east of COVIS is Inferno. The color scale gives the height in meters above the base of COVIS.

Time series having lengths of 2 to 6 minutes were obtained at each station, with sampling frequencies of 4 Hz on two thermistors in the array and 10 Hz on the remaining eight thermistors. In processing, the faster sampling rate was reduced to 4 Hz by decimation. Figure 3 shows the mean and standard deviation of temperature profiles at the seven stations occupied at 1H. The "temperature anomaly" is defined as the difference with ambient temperature and is substantial only up to heights about 50 cm above the seafloor. This maximum height may depend upon ambient current, but no current measurements are available. Measurements of the vertical component of current would be welcome, as the product of temperature anomaly and vertical current is proportional to the vertical component of heat-flux density. It is of particular importance to note that the standard deviation of temperature is very nearly equal to the anomaly. This behavior was noted at all stations having substantial anomaly and is an important element in our inversion algorithm. There is large variability in the magnitude of the temperature anomaly from station to station, and this spatial intermittency must be accounted for in the inversion algorithm.
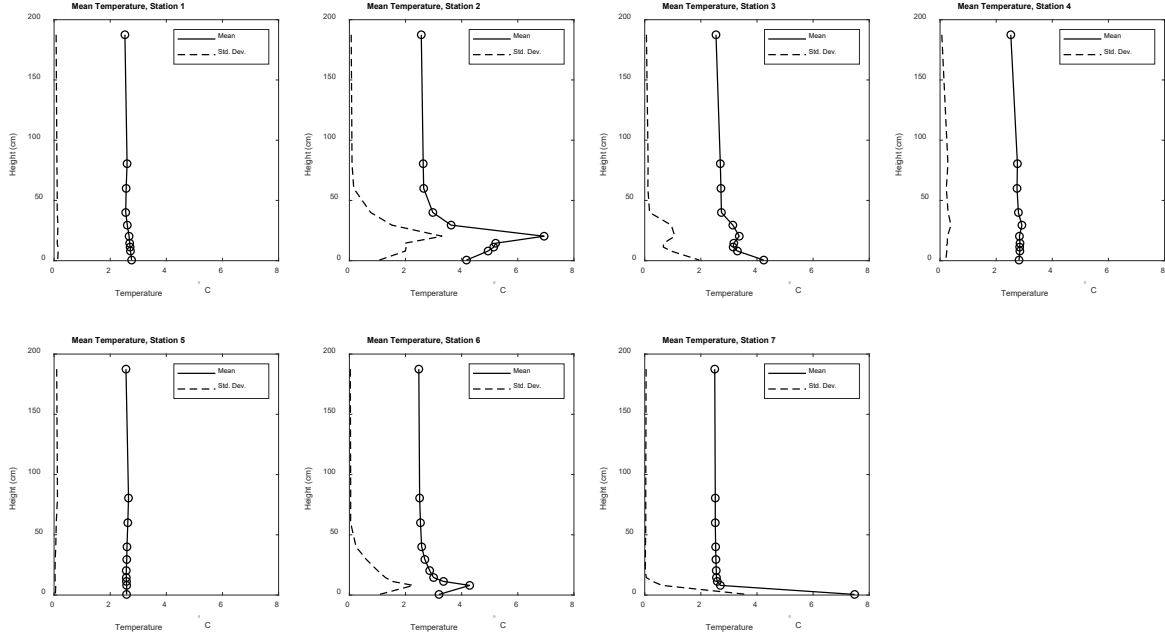
Figure 3. Vertical profiles of mean and standard deviation of temperature at diffuse-flow site 1H. The heights of individual thermistors are marked by circles on the curves for average temperature.

The thermistors are autonomous, with independent sampling, and the drift of the clocks on each unit was sufficient to cause lack of synchronization on the order of a few seconds. As the sonar samples at a rate of 4 Hz, this lack of synchronization is of concern. To assess the magnitude of clock drift, cross-correlations between different thermistors were examined, but no peaks were evident over lags up to 10 s. This leads to the conclusion that the random parts of the time series are essentially independent between thermistors. If the random thermal structure were "frozen" and advected vertically, a strong correlation would be expected at lags determined by the vertical component of velocity and clock offsets due to drift. It is concluded that the thermal structure in space changes on time scales shorter than advection times between thermistors, and that the signature of upward advection is not visible in the thermistor data. In this circumstance, clock drift is of no concern, and statistics appropriate for comparison with inversions of sonar data are estimated as described below.

The first step is to determine the vertically path-averaged temperature difference by summing over vertically-spaced thermistors. A formal definition of path-averaged temperature difference is

$$\Delta T_{pa}(\tau,t) = \frac{1}{H} \int_0^H [T(t,z) - T(t-\tau,z)]dz \qquad (1)$$

The change in temperature between times separated by lag τ is averaged over a vertical path of length H, starting at $z = 0$, the seafloor. This average will later be related to the change in acoustic time-of-flight from the seafloor to the sonar. Even though the acoustic path is not vertical, averages along the slanted acoustic path are equal to those in the vertical if the medium is stratified, with no variation in the horizontal. This is not true at any single time, but will be

approximately true for averages over times long enough to include at least one tidal cycle. The integral in Eq. (1) will be approximated by a discrete sum over the temperatures measured by individual thermistors in the array.

$$\Delta T_{pa}(\tau_i, t_j) = \frac{1}{D} \sum_{m=1}^{M} h_m [T_m(t_j) - T_m(t_j - \tau_i)] \tag{2}$$

Here, m is the index specifying each thermistor in the vertical array, D is the height of the array, and h_m is the spacing between thermistors. While the array height $D = 2$ m is less than the sonar height $H = 4.2$ m, the temperature anomaly is limited to even smaller heights, so it can be assumed that (2) is a reasonable approximation to (1), provided the temperature field is sampled densely enough in the vertical. The structure function needed for comparison with sonar inversions is estimated as the average over time samples of the squared change in temperature difference for lag time τ_i:

$$S(\tau_i) = \frac{1}{J - I} \sum_{j=1}^{J - I_{max}} [\Delta T_{pa}(\tau_i, t_j)]^2 \tag{3}$$

In this expression, I is the largest time sample number available after taking account of the lag τ_i.

An issue arises from the thermal inertia of the thermistors. Even though their response time of 0.1 s is shorter than the sonar sampling interval of 0.25 s, the inversion method to be discussed later is partially dependent on short lags in the structure function, and these are affected by the thermal inertia of the thermistors. To compensate for this, the temperature time series are corrected by dividing their Fourier transforms by a transfer function that is itself a Fourier transform of the response of the thermistor to a unit impulse of temperature. According to the manufacturer, this response can be approximated by an exponential with e-folding time $T = 0.1$ s. The corresponding transfer function is $1/(1 + i\omega T)$. The effect of this correction on the estimated structure function is illustrated in Fig. 4.
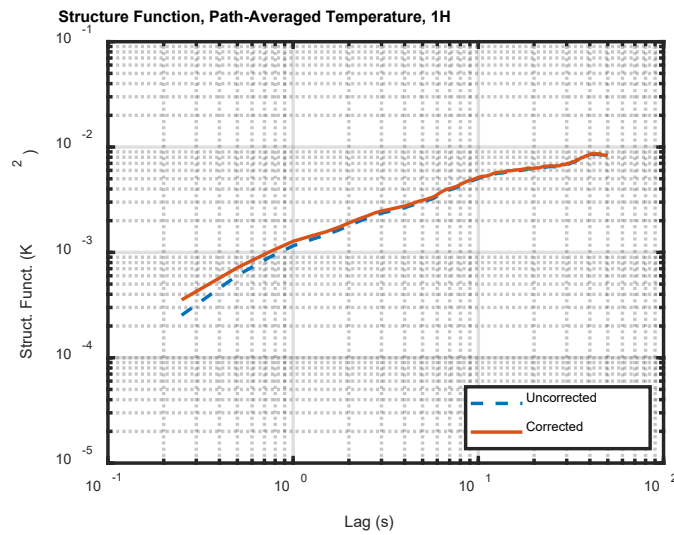

Figure 4. Structure function for path-averaged temperature with and without correction for thermal inertia of thermistors. This is an average over the 7 stations occupied at 1H.

3 Sonar Data

3.1 Sonar system

COVIS is a high-frequency (200 and 400 kHz) sonar system, based on the Reson 7125 multibeam sonar. The source and receiver transducers are mounted on a tripod 4.2 m high on a tri-axial rotator which provides freedom to set pitch, roll, and yaw. COVIS provides near real-time images and monitoring of hydrothermal flow [*Bemis et al.*, 2015]. It employs a wide-vertical-angle transmitter (22º 3-dB full beamwidth at 200kHz) and narrow horizontal-angle (1º 3-dB full beamwidth at 200 kHz) multi-beam receiver with 128º azimuthal coverage. The transmitter and receiver are pitched downward 20º, and three different yaw settings separated by approximately 70º are used to cover three angular "sectors". As in earlier acoustic mapping efforts [*Rona et al.*, 1997], COVIS exploits the expected constancy of ping returns from the seafloor to detect the phase changes caused by travel time variations due to the variable water temperature between COVIS and the seafloor [*Rona and Jones*, 2009]. As there is time jitter between the instant of transmission and beginning of digitization, the transmitted signal that leaks into data channels via cross talk is used to align the phase of successive echo time series. In the typical mode of operation for diffuse-flow study, COVIS transmits a burst of 40 pings (sometimes more) at a rate of 4 Hz, with a burst transmitted every hour or half-hour. The transmitted pulse has an approximately rectangular envelope of width 0.3 ms and a nominal source level of 200 dB re 1 µPa@1m.

3.2 Sonar data processing

COVIS uses digital beamforming in the horizontal with a Hamming window to provide azimuthal resolution of 1º at 200 kHz. For each beam there is a complex (baseband) time series $s_m(t)$ where m is the ping number in the burst. The time series are sampled at a rate of 34 kHz.

The ping-to-ping correlation function is formed using two echo time series $s_1(t)$ and $s_2(t)$ from the same beam, transmitted at "slow" times t_1 and $t_2 = t_1 + \tau$ and with "fast" time arguments t measured from the mid-point of each transmission. Slow time can be regarded as the usual clock time (e.g., UTC), while fast time resets to zero with each sonar transmission. The ping-to-ping correlation estimator is

$$\rho = \frac{|K_{12}|}{\sqrt{K_{11}K_{22}}} \ , \tag{4}$$

where

$$K_{12} = \int_{-\infty}^{\infty} s_1(t)s_2^*(t)w(t-t_0)dt, \tag{5}$$

and with K_{11} and K_{22} being given by similar integrals with the squared magnitude of each echo time series. If the two echo time series are identical, ρ has a value of unity, and if the two are substantially different, ρ will have a magnitude much smaller than unity. The integral in (5) is over fast time with the signal product weighted by a Hamming window function $w(t)$ whose position time, t_0, determines path length ("slant range"), $r = ct_0/2$, and whose width (1.5 ms)

is set by a trade-off between range resolution and the desire to reduce statistical fluctuations. The integral is performed as a sum over samples in the time domain. The estimate provided by Eq. (4) is averaged over all the data available for a 24-hour period. This rather long period was chosen in order to average over tidal effects, which will be discussed in Sect. 6. COVIS was programmed to obtain diffuse-flow data either every one-half hour or every hour. Except for occasional data loss, 24 or 48 such estimates are averaged. For each day, averaged ping-to-ping correlation is computed for 38 lag times with spacing 0.25 s, for all 128 sonar beams, and for ranges out to 30 m with an interval of 0.56 m between placement of the Hamming window in range. These results, originally in a polar coordinate system, are interpolated onto a 2D rectangular grid with 0.5-m spacing in both dimensions. In this gridding process, the bathymetry as measured by COVIS is taken into account in converting the coordinates (azimuthal angle and slant range to seafloor) to x- and y-coordinates.

3.3 Structure Function

As a first step toward inversion, a relation between ping-to-ping correlation and the temperature structure function will be sought. Changes in sound speed cause changes in the sonar echo from the seafloor quantified by the ping-to-ping correlation. There is a simple linear relationship between temperature change ΔT and sound-speed change Δc. For this work, $dc/dT = 4.37$ ms^{-1}K^{-1} is used, appropriate for nominal temperature 2.4º C, salinity 34.5 psu, and depth 1440 m. Salinity fluctuations have a negligible effect, as a salinity change of about 15 psu would be required to match the sound-speed change caused by a (plausible) 5º temperature change. Current fluctuations have no short-term effect on the sonar signal, as time shifts due to this mechanism are cancelled over the round-trip acoustic path. Of course, currents do transport and alter the turbulent temperature structure, contributing to ping-to-ping change in the sonar signals.

It is not feasible to obtain a closed-form model for the expected value of the estimator ρ, as Expression (4) is an irrational functional of the two time series. In previous work [*Jackson et al.,* 2017], we employed a formal approximation, but lack of any measure of the bias that might result from this approximation motivates a new approach. In this approach, Monte Carlo simulations (described later in this article) are used to generate synthetic sonar signals using a point-scatterer model.

The time-of-flight for a sonar signal to travel to a point on the seafloor and back to the sonar is

$$t_1 = 2\int_0^r \frac{dr}{c_1} \tag{6}$$

for ping 1, with the integral being along the nearly straight path of length r shown in Fig. 5. At a later time, the position-dependent sound speed will have changed from c_1 to $c_2 = c_2 + \Delta c$, and the time-of-flight for ping 2 will be altered to

$$t_2 = t_1(1-\alpha) \tag{7}$$

where

$$\alpha \approx \frac{1}{cr}\int_0^r \Delta c\, dr \ . \tag{8}$$

In deriving this expression ray bending is neglected, based on ray-tracing simulations showing that refractive effects are negligible in the circumstances of interest. The parameter c is a nominal, position-independent sound speed, and

$$\Delta c = c_2 - c_1 \tag{9}$$

is dependent on position along the path and is assumed to have absolute value much smaller than c. The model neglects dependence upon coordinates parallel to the seafloor within the sonar resolution cell, thus Δc must be interpreted as an average over these coordinates.
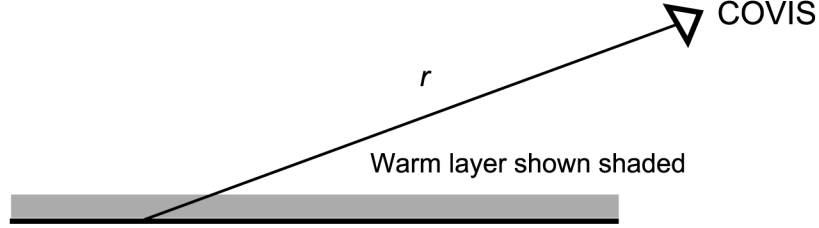

Figure 5. Geometry for sonar measurement of a diffuse-flow region. The line-of-sight path length r is indicated.

Next, consider how the time scaling (7) caused by sound-speed change affects the second echo signal $s_2(t)$ relative to the first, $s_1(t)$. Treating the sonar and environment as a time-invariant system (invariant over the very short round-trip acoustic travel time), one can write

$$s_1(t) = \int_{-\infty}^{\infty} s_0(t')e^{i\omega_0 t'}g(t-t')dt' \ , \tag{10}$$

where $g(t)$ is the "impulse response" of the combined sonar-environment system at the time of the first transmission, $s_0(t)$ is the envelope of the transmitted signal, and ω_0 is the center frequency of the sonar in rad/s. The impulse response incorporates the complexity of scattering by the seafloor as well as the effects of acoustic transmission and sonar properties. Due to the time scaling shown in (7), the second echo is

$$s_2(t) = \int_{-\infty}^{\infty} s_0(t')e^{i\omega_0 t'}g(t-\alpha t-t')dt' \ . \tag{11}$$

For the Monte Carlo calculations, the impulse response is constructed by assuming point scatterers having random, zero-mean, Gaussian-distributed scattering amplitudes and random locations on a flat seafloor. Each scatterer contributes a scaled, delayed copy of the transmitted signal to the final synthesized echo signal. To account for the observed spatial intermittency of the diffuse-flow regions at ASHES, only a fraction of the scatterers at the center of the simulation seafloor patch (referred to later as the "hot spot") are subject to sound-speed change, which is measured by α defined above. The relevant measure of intermittency will be denoted F, and is the fraction of the 1.5-ms window width over which the sound-speed change is applied. This fraction is adjusted to fit ground-truth thermistor data. The parameter α is changed randomly for each Monte Carlo realization and is drawn from a zero-mean Gaussian distribution. In order that the horizontally averaged, path-averaged sound-speed change have the standard deviation $c\sigma_\alpha$, the standard deviation of α over the hot spot is assigned the value σ_α/F.

9

The Monte Carlo calculations produced synthetic data comprising 400 echo-pair realizations. These were generated with Gaussian-distributed α with 40 different standard deviations at 7 different ranges out to 34 m. Thus 7x2x400x40 = 224000 synthetic signals are generated. The range dependence of correlation was negligible, so correlation was averaged over both range and realizations. The average ping-to-ping correlation was fitted by an algebraic function, with results shown in Fig. 6. This curve is for $F = 0.15$, a value found by fits of sonar inversion of synthetic data to thermistor data as discussed later in this article. The algebraic function is then inverted to give an expression for the standard deviation of α in terms of average correlation. Referring to Fig. 6, the decorrelation, $1 - < \rho >$, is proportional to the square of σ_α for small σ_α. As σ_α grows, $< \rho >$ approaches a constant, non-zero, asymptote. It is important to realize that the σ_α on the x-axis of Fig. 6 represents the spatial average of the normalized, path-averaged sound-speed standard deviation. As such it is smaller than the standard deviation within the hot spot.
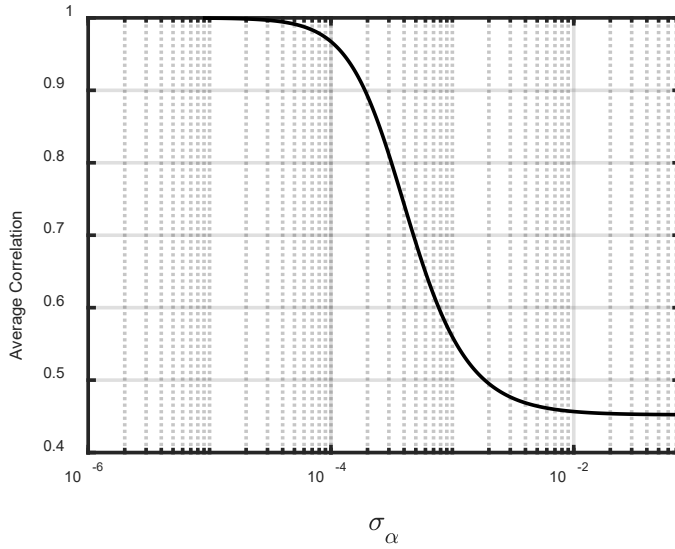

Figure 6. Average correlation obtained from Monte Carlo simulations. The abscissa is the standard deviation of normalized, path-averaged sound-speed change.

The path-averaged sound-speed change is

$$\Delta c_{pa} = \alpha c = \frac{1}{r} \int_0^r \Delta c \, dl \, . \tag{12}$$

It follows that the inversion method allows an estimate of path-averaged temperature change,

$$\Delta T_{pa} = \Delta c_{pa} / (dc / dT). \tag{13}$$

Given that path-averaged temperature change, rather than path-averaged temperature itself is estimated, a natural statistical characterization is provided by the structure function (3) and here expressed as

$$S(\tau, t_s) = < [\Delta T_{pa}(\tau, t_s)]^2 >, \tag{14}$$

where t_s is a slow-time variable. The variable τ is the time difference between the two pings being compared. The brackets $<>$ denote a formal average over a hypothetical infinite ensemble

10

but will be implemented as a sample average over one day's data. Note that the structure function is simply the second moment of path-average temperature change occurring after an elapsed time τ, which will be referred to as "lag." As temperature change is proportional to sound-speed change, (14) is equivalent to

$$S(\tau, t_s) = \left(\frac{c}{dc/dT}\right)^2 \sigma_\alpha^2. \tag{15}$$

This is the expression that is used to estimate the structure function for path-averaged temperature. Recapping, the cross correlation between pings separated in time by τ is computed using Expression (1). The cross correlation is averaged over the 24 or 48 separate transmissions for each day, and the expression illustrated in Fig. 6 is used to obtain σ_α. Finally, (15) is used to obtain the temperature structure function over the range of lags $0 < \tau < 10$ s.

To facilitate inversion for heat flux density, the following three-parameter fit is made to the structure function for path-averaged temperature:

$$S(\tau) = 2\sigma_T^2[1 - e^{-(\tau/\tau_0)^\mu}] , \tag{16}$$

where σ_T^2 is the variance of path-averaged temperature fluctuations, τ_0 is a time scale, and μ is an exponent giving the power-law behavior at small lags. The covariance for path-averaged temperature fluctuations in terms of the fitting parameters is

$$K_T(\tau, t_s) = \sigma_T^2 e^{-(\tau/\tau_0)^\mu} , \tag{17}$$

Figure 7 gives an example of the fitting of the acoustically estimated structure function for path-averaged temperature for Site H-1 by Expression (16).
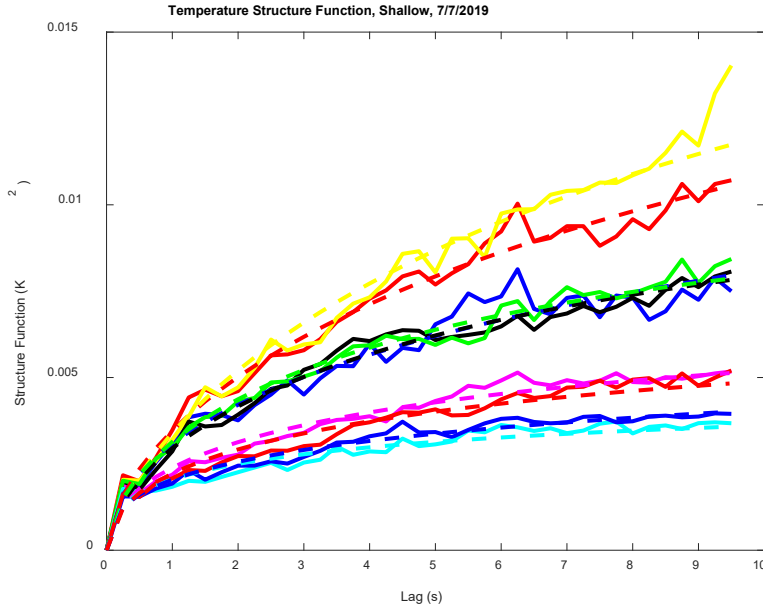

Figure 7. Structure function and three-parameter fit for path-averaged temperature structure function estimated from sonar data. Nine adjacent grid points at Site 1H are displayed for 7 July, 2019.

11

4 Comparison of Thermistor and Sonar Data

The first step in validation of the inversion method is comparison of the sonar-derived structure function with that obtained from thermistor data. For this, sonar data from 7 July 2019, the day after thermistor data were obtained, were used assuming the fractional area occupied by diffuse venting is $F = 0.15$. Figure 8 shows the comparison for the two sites of interest, with the thermistor results shown as circles, and the sonar results shown as solid curves. The sonar curves are obtained from a 24-hour average of ping-to-ping correlation. Navigational error in placing the thermistor measurement sites with respect to COVIS coordinates could be as large as 2 m. To accommodate this, the mean (solid curves) and sample standard deviation (error bars) of 25 sonar-derived structure functions from within a 2.5-m x 2.5-m area have been computed and plotted. These standard deviations represent the spatial variability of the inversion which, in agreement with visual observation, is large. This variability translates navigational error into uncertainty that compromises comparison of thermistor and sonar data. To obtain the thermistor statistics, Expression (3) is evaluated for each station, and the statistical error in each of these estimates is neglected, as the number of time samples is very large in comparison to the number of stations. The thermistor estimates (red circles) are averages over all stations with error bars that are the sample standard deviations divided by the square root of the number of stations (7 for 1-H, 11 for 4-C).
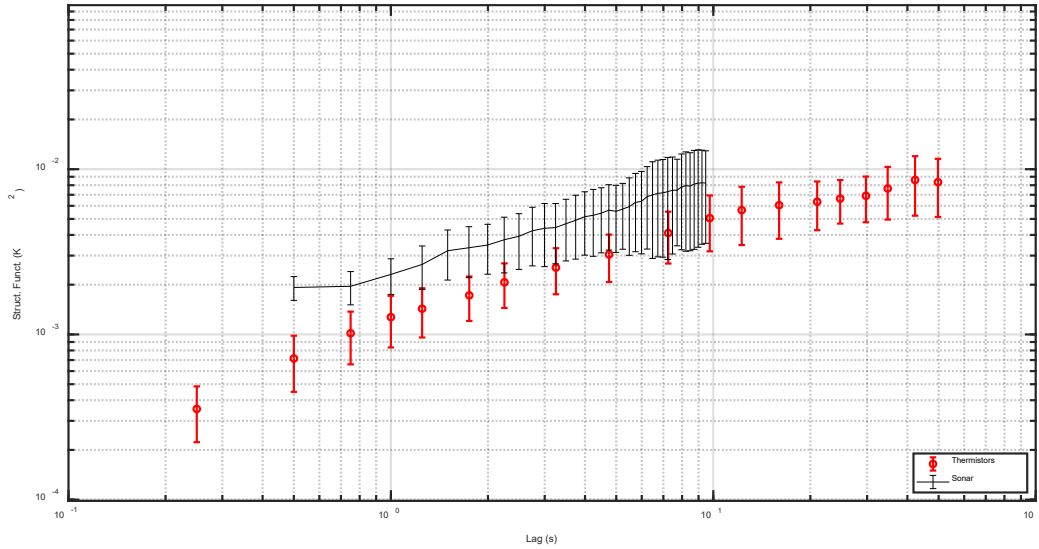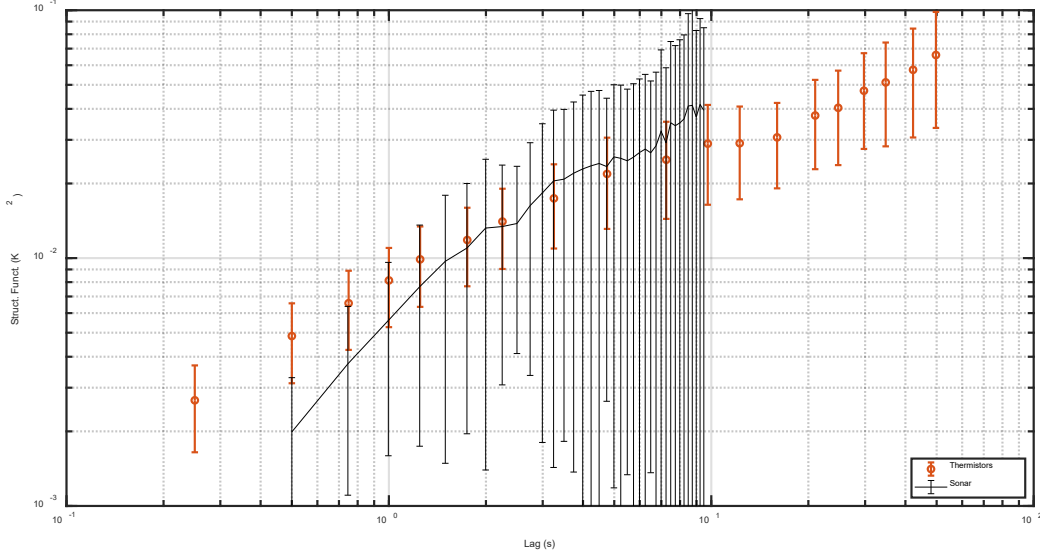
Figure 8. Comparison of structure function for vertically integrated temperature structure estimated from sonar and thermistor data. Upper panel, site 1H, lower panel, site 4C. The black error bars depict the spatial variability of the inversion over 2.5-m x 2.5-m squares, while the red error bars represent the standard deviations of the estimates of the structure function using thermistor data.

The comparison of sonar and thermistor results is satisfactory, although there is a mismatch for the shortest lags for Site 1H. This site had a rather low level of hydrothermal activity compared to site 4C, and it appears that the flattening of the sonar-derived structure function at small lags indicates a "floor" below which good estimates are not possible. This floor is most likely due to random thermal structure in the water column, due to wafting of the focused flows of Mushroom and Inferno. The spatial variability for the sonar inversion at Site 4C is very large, indicating strong spatial intermittency with concomitant sensitivity to navigational error. The large downward extent of the error bars representing this variability results from the standard deviation approaching or exceeding the sample mean, and is exaggerated by the use of a logarithmic vertical scale. As noted above, it is assumed that the fractional area occupied by diffuse venting is $F = 0.15$. As this fraction is increased, the sonar curves move upward, and as it is decreased, they move downward. The value $F = 0.15$ gives consistency between thermistor and sonar estimates at the two sites and is used in inversions to be shown later. It is encouraging that a single choice of F gives reasonable agreement between sonar- and thermistor-derived structure functions at two different sites. While F must vary to some extent with location at scales larger than the resolution of the inversion, it seems reasonable to assume that the chosen value of F represents a spatial average. This choice of F is the first step in the inversion method. Having a value for F, the relation between ping-to-ping correlation and the structure function is established. With this relation, the sonar data provide structure function estimates. Each estimate, for each point on the 2D grid, is reduced to 3 numbers by fitting the analytic expression (16). Finally, as described in the following section, two of these three numbers are used in estimating the heat-flux density for each point on the grid.

13

5 Inversion Algorithm

The heat-flux density, q, in W/m^2, is proportional to the product of average vertical velocity, w, and the average of the temperature anomaly T_{anom}:

$$q = w c_{vp} < T_{anom} > , \qquad (18)$$

where c_{vp} is the heat capacity per unit volume at constant pressure. As noted in Sect. 2, the temperature anomaly is approximately equal to the standard deviation of temperature,

$$\sigma_T = < T_{anom} > . \qquad (19)$$

The sonar inversion gives the standard deviation of path-averaged temperature, which can be expressed as

$$\sigma_{Tpa} = \sigma_T d / D , \qquad (20)$$

where d is the effective thickness of the warm layer, and D is the height of the sonar (4.2 m). The sonar inversion also provides a characteristic time, τ_0, that quantifies the time required for the temperature field to undergo significant change. As the path-averaged temperature is dominated by the largest scales of the random temperature field, it seems reasonable to assume that these scales are of order d, and that the vertical velocity is

$$w = d / \tau_0 . \qquad (21)$$

Combining (18)-(21), the heat-flux density is

$$q = c_{vp} \sigma_{Tpa} D / \tau_0 . \qquad (22)$$

Only two of the three parameters produced by the inversion for the structure function appear in Expression (22). The use of the temperature standard deviation needs no further justification, but the omission of the exponent parameter μ can be justified because τ_0 is the lag time for which the structure function attains a value equal to 1-1/e of its asymptote, irrespective of the value of μ. This is an empirical model, and it is likely that (22) would be modified by multiplication by a constant of order unity as a result of future comparison of sonar-derived heat-flux density with direct measurements.

6 Inversion Results

Figure 9 is an example of the application of Expression (22) to obtain heat-flux density from COVIS data. The two images are formed from a combination of data from the three different azimuthal sectors with ping-to-ping correlation averaged over the period 00:00 to 24:00 UTC on July 7, 2019 and July 11, 2019. This rather long averaging period is intended to reduce the effect of tidal currents on the heat-flux estimates. Xu et al. (2021) have shown that tidal effects on sonar diffuse-flow data are significant. In forming Fig. 9, data have been deleted at ranges deemed too short or too long to give reliable values for ping-to-ping correlation. Data have also been deleted in regions near the Mushroom (M) and Inferno (I) black smokers. These deletions are necessitated by shadowing of the seafloor, whether by the sulfide structures or the focused plumes, which wander in angle in response to currents.
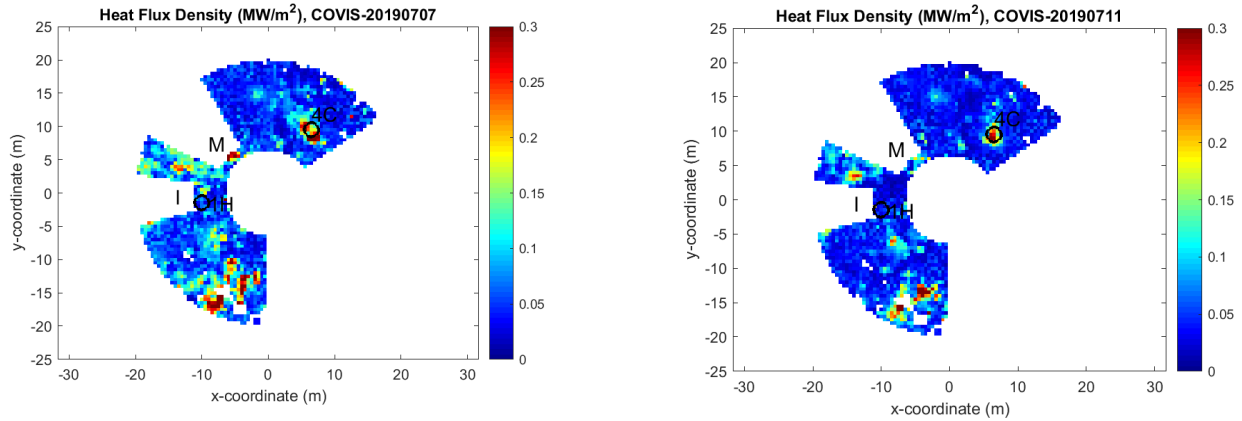
Figure 9. Heat-flux density in MW/m² as determined using Expression (22), with ping-to-ping correlation averaged over the period 0:00 to 23:30, UTC July 7, 2019 (Left panel) and July 11, 2019 (Right panel). Data have been deleted in the vicinity of the Mushroom (M) and Inferno (I) smokers. Ground-truth thermistor data were taken at Sites 1H and 4C, noted on the plots.

The two images show appreciable differences, with more activity evident on July 7 than July 11. These could be artifacts caused by either the Inferno or Mushroom plumes, as interposition of a plume between the sonar and the seafloor might cause inactive regions to appear active, as noted later. The ground-truth sites are marked in Fig. 9, and it is apparent that activity at 1H is much lower than at 4C, consistent with thermistor measurements and Fig. 8.

A time series of heat output has been formed by integrating the heat-flux density (obtained from daily averages of the ping-to-ping correlation) over area and dividing the result by area to obtain average heat-flux density. The yaw rotator motor failed on 24 November 2019 with the result that data gathering at later times was restricted to Sector 1 which includes the Mushroom and Inferno vents. As a consequence, the time series presented in Fig. 10 is restricted to Sector 1 with the deletions noted in connection with Fig. 9. In the time before failure of the yaw motor, the sonar azimuthal pointing direction showed occasional changes which resulted in abrupt changes in estimated heat flux. In response, the time series displayed in Fig. 10 is further restricted to times after the yaw motor failure, ensuring that the pointing direction was constant. The time series shows no evident trends over the period 24 November 2019 through 27 April 2021.

The cause of the time variation seen in the upper panel of Fig. 10 is unknown. It may be either due to actual variation in heat output, or it may be an artifact caused by tidal currents. Our efforts to compare the heat-flux density time series with pressure and current time series have been inconclusive, but more effort in this direction is warranted. Sample averages over the heat-flux density shown in the figure yield 285 ± 43 kW m^{-2}. If it is assumed that the variation seen in Fig. 10 does not represent actual variation in heat output, then the standard deviation 43 kW m^{-2} can be taken as the uncertainty in heat-flux estimates from one-day's worth of data.
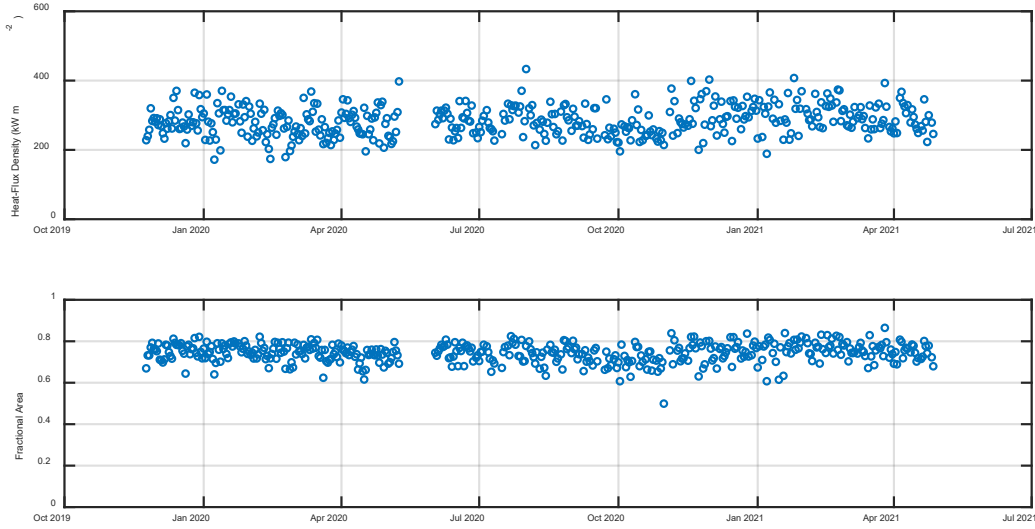
Figure 10. Upper panel: Time series average heat-flux density over Sector 1. Lower panel: Time series for fractional active area.

The lower panel of Fig. 10 is a time series for "fractional area", which is defined as follows. First the "active area" is defined as

$$A_{active} = \frac{(\int_S q(x,y)dx\,dy)^2}{\int_S q^2(x,y)dx\,dy}. \tag{23}$$

This definition gives a value that is equal to the total area included in the heat-flux image

$$A = \int_S dx\,dy, \tag{24}$$

if the heat-flux density is constant over the entire area. If the heat flux vanishes everywhere except on patches that occupy an area A_p, where it takes on a single value for all patches, definition (23) yields the intuitive value $A_{active} = A_p$. The fractional area plotted in Fig. 10 is A_{active}/A. It typically ranges between 0.7 and 0.8, showing that the heat flux density obtained by inversion is not concentrated in a few small patches, but spread significantly. This conflicts with video observations that the diffuse-flow patches are quite localized. We attribute this, at least in part, to the effect of currents and the use of averaging over a 24-hour period for each data point in Fig. 10. There is no conflict with the assumed fractional active area of 0.15 assumed in Sect. 3.3, as this fraction refers to the fine-scale distribution of activity, unresolvable by the inversion method. Figure 11 shows that there is a definite correlation between fractional active area and heat-flux density, with fractional area increasing as heat-flux density increases. This may indicate that a part of the inverted heat flux is an artifact, caused by wafting of the focused

16

plumes into the sonar's lines-of-sight, or it may simply indicate that increased activity involves an increased area of the seafloor. Wafting of the focused plumes would cause inactive areas to appear active, increasing fractional area. At present we have no means of correcting for the bias that would result from such an artifact if, in fact, it occurs.
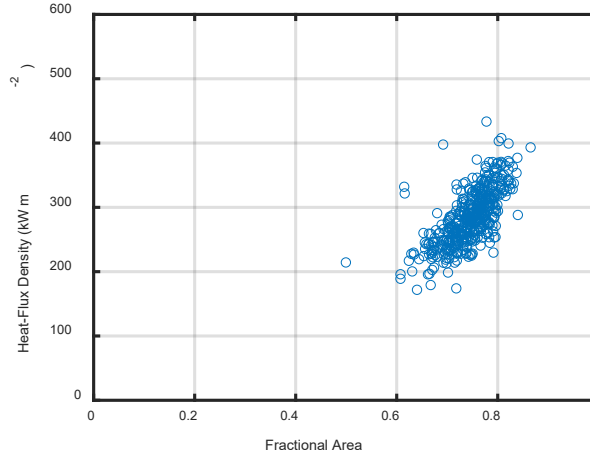

Figure 11. Average heat-flux density over Sector 1 vs. fractional active area.

Rona and Trivett [1992] made heat-flux measurements at ASHES, and their nearest diffuse-flow region had area 962 m^2 and estimated heat flux density 57 kW/ m^2. Our value averaged over COVIS' 567 m^2 field of view (combining all three sectors) is 187 kW/ m^2 for 7 July 2019. The mean of the time series of Fig. 10 is 285 kW/ m^2 for sector 1, with area 233 m^2 after deleting regions near Mushroom and Inferno. The statistical error in this number is only 2 kW/ m^2 owing to the large number (443) of samples. The systematic error is unknown but expected to be a number of order unity times this mean. Given the 1:5 ratio of the uncertainty bounds given by Rona and Trivett, their estimate does not help with calibration of our method, although the two measurements are consistent.

7 Conclusions

A method has been developed to estimate the heat output of diffuse hydrothermal flows using multibeam sonar data. Temperature fluctuations modulate seafloor echoes, so that ping-to-ping correlation can be used to estimate properties of the random temperature field from which heat-flux density can be obtained. The method is essentially empirical, and calibration by comparison with directly measured heat flux in a future field exercise would be very useful. Even without calibration, the method provides estimates of heat-flux density up to an unknown factor of order unity. These estimates are consistent with historical data and are given as maps over the sonar field-of-view, with one such map per day. A time series over the period 24 November 2019 through 27 April 2021 shows no significant trends in heat flux.

Data Availability Statement

The COVIS and thermistor-array data presented in this paper are available at
https://oceanobservatories.org/pi-instrument/cabled-array-vent-imaging-sonar-covis/.

References

Barreyre, T., J. Escartin, R. Garcia, M. Cannat, E. Mittelstaedt, and R. Prados, R. (2012), Structure, temporal evolution, and heat flux estimates from the Lucky Strike deep-sea hydrothermal field derived from seafloor image mosaics, Geochemistry, Geophysics, Geosystems, 13(4).

Bemis, K., R. Lowell, and A. Farough (2012), Diffuse flow on and around hydrothermal vents at mid-ocean ridges, Oceanography, 25(1), 182-191, http://dx.doi.org/10.5670/oceanog.2012.16 2012.

Bemis, K.G., D. Silver, G. Xu, R. Light, D. Jackson, C. Jones, S. Ozer, S., and L. Liu (2015), The path to COVIS: A review of acoustic imaging of hydrothermal flow regimes. Deep Sea Research Part II: Topical Studies in Oceanography, 121, 159-176, doi:10.1016/j.dsr2.2015.06.002.

Jackson, D.R., A.N. Ivakin, G. Xu, and K.G. Bemis (2017), Sonar observation of diffuse hydrothermal flows, Earth and Space Science, 4, 230-239.

Mittelstaedt, E., Fornari, D.J., Crone, T.J., Kinsey, J., Kelley, D. and Elend, M., 2016. Diffuse venting at the ASHES hydrothermal field: Heat flux and tidally modulated flow variability derived from in situ time-series measurements. *Geochemistry, Geophysics, Geosystems*, *17*(4), pp.1435-1453.

Pruis, M.J. and Johnson, H.P., 2004. Tapping into the sub-seafloor: examining diffuse flow and temperature from an active seamount on the Juan de Fuca Ridge. *Earth and Planetary Science Letters*, *217*(3-4), pp.379-388.

Rona, P.A., and D.A. Trivett (1992), Discrete and diffuse heat transfer at ASHES vent field, Axial Volcano, Juan de Fuca Ridge, Earth and Planetary Science Letters, 109:57-71.

Rona, P.A., D.R. Jackson, T. Wen, K. Mitsuzawa, C. Jones, K.G. Bemis, and J.G. Dworski (1997), Acoustic mapping of diffuse flow at a seafloor hydrothermal site: Monolith Vent, Juan de Fuca Ridge, Geophys. Res. Letters, 24:2351-2354.

Rona, P. A, and C.D. Jones (2009), Acoustic scintillation thermography, Encyclopedia of Ocean Sciences (Second Edition), Elsevier Ltd., doi:10.1016/B978-012374473-9.00735-9.

Rona, P.A., K.G. Bemis, G. Xu, and K. Mitsuzawa (2015), Estimations of heat transfer from Grotto's NorthTower: A NEPTUNE Observatory case study, Deep-Sea Research II, 121, 95-111, http://dx.doi.org/10.1016/j.dsr2.2015.05.010.

Schultz, A., J. Delaney, J., and R. McDuff (1992), On the partitioning of heat flux between diffuse and point source seafloor venting, J. Geophys. Res., 97(B9), 12299-12314.

Trivett, D.A. and A.J. Williams III (1994), Effluent from diffuse hydrothermal venting 2. Measurements of plumes from diffuse hydrothermal vents at the southern Juan de Fuca Ridge, J. Geophys. Res., 99(C9), 18417-18432.

Veirs, S.R. R.E. McDuff, and F.R. Stahr (2006), Magnitude and variance of near-bottom horizontal heat flux at the Main Endeavour hydrothermal vent field, Geochem. Geophys. Geosyst., 7, Q02004, doi:10.1029/2005GC000952.

Xu, G., K.G. Bemis, D.R. Jackson, and A.N. Ivakin (2021), Acoustic and in-situ observations of deep seafloor hydrothermal discharge: an OOI Cabled Array ASHES Vent Field Case Study, Earth and Space Science, 8, e2020EA001269. https://doi.org/10.1029/2020EA001269